https://doi.org/10.5194/essd-2026-901
Preprint. Discussion started: 17 November 2026
© Author(s) 2026. CC BY 4.0 License.



Open Access Earth System Science Data Discussions

# A ground-based multi-instrument remote sensing dataset of in-cloud vertical air motion, particle terminal fall velocity, and hydrometeor classification over Xi'an, China (2021–2022)

Huige Di, Yun Yuan, Shuling Hu, Ning Chen, Yufeng Wang, Qing Yan, Dengxin Hua*

School of Optoelectronic Science and Intelligent Instrumentation, Xi'an University of Technology, Xi'an, China

Correspondence: Dengxin Hua (dengxinhua@xaut.edu.cn)

Continuous ground-based remote sensing observations were conducted at the Jinghe National Meteorological Observation Station in Xi'an, China, during 2021–2022. Using measurements from a Ka-band millimeter-wave cloud radar (MMCR) and a microwave radiometer (MWR), we developed an integrated cloud observation dataset with high temporal and vertical resolution. The MMCR provides radar reflectivity factor ($Z_e$), mean Doppler velocity ($V_D$), Doppler spectral width ($SW$), signal-to-noise ratio (SNR), and Doppler power spectra; Doppler spectra are used to retrieve in-cloud vertical air velocity ($w$), from which particle terminal fall velocity ($V_t$) is derived, while radar variables and temperature are used to identify seven hydrometeor classes: Snow, Ice, Mixed, Supercooled liquid water (SCL), Warm droplets, Drizzle, and Rain. The final dataset covers 541 valid observation days, with a temporal resolution of 5 s and a vertical grid spacing of 30 m. The products are provided on a common time–height grid and support studies of cloud dynamical–microphysical interactions, cloud-to-precipitation transitions, remote sensing algorithm evaluation, and model validation over continental midlatitude regions. The dataset is publicly available through ScienceDB at https://doi.org/10.57760/sciencedb.016rz. (Di et al., 2026)

**Keywords:** Ka-band millimeter-wave cloud radar; Doppler power spectra; vertical air motion; particle terminal fall velocity; hydrometeor classification; long-term observational dataset

## 1. Introduction

The formation, growth, phase transitions, and sedimentation of hydrometeors are closely coupled with in-cloud air motions, jointly governing the cloud life cycle and the transition from clouds to precipitation. Continuous observations of these processes require not only information on cloud location, thickness, and echo intensity, but also estimates of $w$, $V_t$, and the distribution of different hydrometeor types within clouds.

Aircraft in situ measurements provide direct information on cloud particle size, shape, and motion, but limitations in flight duration, flight paths, and sampling coverage make it difficult to obtain continuous, long-term vertical observations. Ground-based remote sensing systems combining millimeter-wave cloud radar (MMCR), light detection and ranging (lidar), and microwave radiometer (MWR) measurements provide continuous observations of clouds and light precipitation at high temporal and vertical resolution, supporting studies of cloud and precipitation vertical structure, changes in hydrometeor types, and particle dynamics. The development of Cloudnet and similar observational and processing frameworks has demonstrated that multi-instrument observations can generate higher-level products, including cloud macrophysical properties, target classification, and microphysical parameters, from basic remote sensing measurements, providing standardized datasets for model evaluation and cloud process studies (Illingworth et al., 2007). Recent ground-based remote sensing datasets have increasingly incorporated multi-instrument observations, consistent quality control, and higher-level geophysical products beyond basic

https://doi.org/10.5194/essd-2026-901
Preprint. Discussion started: 17 November 2026
© Author(s) 2026. CC BY 4.0 License.



Open Access Earth System Science Data Discussions

measurements from individual instruments (Acquistapace et al., 2022; Chellini et al., 2023; Ferrone and Berne, 2023; Tukiainen et al., 2025). For example, the Pallas Cloud Experiment (PaCE) 2022 combined ground-based remote sensing measurements and auxiliary data to derive ice water content, ice effective radius, and target classification products, illustrating the development of datasets that integrate cloud macrophysical and microphysical properties from continuous observations.

In ground-based remote sensing, vertically pointing MMCRs are sensitive to cloud particles and provide continuous measurements of conventional radar moments, including radar reflectivity factor ($Z_e$), mean Doppler velocity ($V_D$), and Doppler spectral width ($SW$) (Kollias et al., 2007a, b; Görsdorf et al., 2015; Liu et al., 2017). These moments are derived from Doppler spectra through integration or statistical calculations and characterize radar echo intensity and bulk motion, but they contain less information about particle populations across the Doppler velocity spectrum. Doppler power spectra retain the distribution of backscattered power across Doppler velocities, providing additional information on air motion, particle sedimentation, particle populations, and spectral broadening. Extending the analysis from conventional radar moments to Doppler spectra can improve the characterization of cloud dynamics and microphysical processes using MMCRs (Kollias et al., 2002, 2011a, b; Shupe et al., 2004, 2008b; Luke and Kollias, 2013; Liu et al., 2014; Yu et al., 2014; Vogl et al., 2024).

One important application of Doppler spectra is to separate the contributions of vertical air motion and hydrometeor sedimentation to the observed Doppler velocity. For vertically pointing MMCRs, $V_D$ includes contributions from both vertical air motion and hydrometeor sedimentation relative to the surrounding air and therefore cannot directly represent $w$. Early studies used spectral signals from small cloud droplets, which have low terminal fall velocities and approximately follow air motion, as tracers to estimate $w$ (Gossard, 1994; Kollias et al., 2001; Shupe et al., 2008a, b; Bühl et al., 2015). Shupe et al. (2008b) further accounted for spectral broadening caused by turbulence, wind shear, and radar beamwidth. Zheng et al. (2017) applied the small-particle tracing method to Ka-band cloud radar Doppler spectra to retrieve $w$ in convective clouds, while other studies used multiple radars or combined observations to constrain vertical air motion in complex cloud systems (North et al., 2017; Williams et al., 2016). Once $w$ is retrieved, $V_t$ can be estimated by removing the air-motion contribution from $V_D$ (Radenz et al., 2018).

The shape and multimodal structure of Doppler spectra also provide information on particle populations and hydrometeor types. When particle populations with different scattering and sedimentation characteristics coexist within an MMCR sampling volume, they may produce distinct spectral peaks or branches. Doppler spectral analysis has progressed from extracting individual spectral peaks and edges to identifying multiple peaks and separating particle populations. Vogl et al. (2024) developed the PEAKO–peakTree method to identify and organize subpeaks in MMCR Doppler spectra and retrieve spectral moments for individual particle populations, demonstrating that populations such as liquid cloud droplets can be identified based on their peak reflectivity and velocity characteristics. Previous studies have also combined Doppler spectral information with hydrometeor classification and mixed-phase cloud identification to distinguish liquid cloud droplets, ice particles, and particle populations with different sedimentation characteristics (Peng et al., 2011; Shupe et al., 2004; Bühl et al., 2016; Yu et al., 2014; Yuan et al., 2024). These spectra therefore provide information on particle populations in addition to the radar moments and retrieved velocities.

https://doi.org/10.5194/essd-2026-901
Preprint. Discussion started: 17 November 2026
© Author(s) 2026. CC BY 4.0 License.





Long-term archives of Doppler spectra suitable for reprocessing, together with corresponding higher-level retrieval products, remain limited. Existing long-term cloud radar archives and publicly available datasets commonly provide conventional products such as $Z_e$, $V_D$, $SW$, and target classification, whereas studies using Doppler spectra have focused mainly on algorithm development, individual cloud cases, or specific cloud types, including $w$ retrieval, cloud–drizzle separation, and complex spectral peak identification. Consistent processing of Doppler spectra over extended observation periods to generate integrated products of $w$, $V_t$, and hydrometeor classification remains uncommon (Liu et al., 2019; Yuan et al., 2025). Existing ESSD datasets based on ground-based remote sensing demonstrate the value of multi-instrument observations and standardized higher-level products for data reuse (Chellini et al., 2023; Tukiainen et al., 2025). The present dataset addresses this gap by providing consistently processed velocity and hydrometeor products on a common time–height grid.

In this study, we compiled continuous ground-based remote sensing observations collected at the Jinghe station in Xi'an, China, during 2021–2022 to develop a dataset of cloud observations and retrievals based on vertically pointing Ka-band MMCR measurements and MWR temperature profiles. The dataset comprises three groups of products: (1) basic radar measurements, including $Z_e$, $V_D$, $SW$, and signal-to-noise ratio (SNR), together with temperature ($T$); (2) $w$ and $V_t$ derived from Doppler power spectra; and (3) hydrometeor classification obtained by combining radar variables with temperature constraints. The dataset aims to convert information retained in long-term MMCR Doppler spectra but not fully captured by conventional radar moments into reusable products linking cloud dynamics, particle sedimentation, and hydrometeor types, providing observations for studies of cloud dynamical–microphysical interactions, cloud-to-precipitation transitions, remote sensing algorithm evaluation, and atmospheric modeling over continental midlatitude regions.

This paper describes the observational basis, processing workflow, and product generation methods of the dataset and assesses data coverage, product completeness, and the main statistical characteristics for 2021–2022. We first describe the observation site and instruments, followed by radar quality control, $w$ and $V_t$ retrieval, and hydrometeor classification methods; we then characterize the dataset using a representative case, long-term probability distributions, vertical profiles, hydrometeor-conditioned statistics, seasonal variability, and interannual consistency, and assess the internal consistency and statistical sensitivity of the velocity products through arithmetic consistency checks and systematic perturbation tests.

## 2. Observation site and instrumentation

### 2.1 Observation site

Continuous ground-based remote sensing observations were conducted at the Jinghe National Meteorological Observation Station (34°26′ N, 108°58′ E; approximately 411 m above sea level; Fig. 1a) in Xi'an (33°42–34°45′ N, 107°40–109°49′ E), Shaanxi Province (31°42–39°35′N, 105°29–111°15′E), China. The station is located at the central Guanzhong Plain, between the Loess Plateau to the north and the Qinling Mountains to the south, within a mountain–plain transition region. The station location and surrounding topography are shown in Fig. 1a).

Several ground-based remote sensing instruments are deployed at the Jinghe station, of which the colocated Ka-band MMCR and MWR provide the primary measurements used in this dataset. The two instruments are separated by approximately 3 m horizontally (Fig. 1b), allowing active and passive remote sensing measurements of nearly the

https://doi.org/10.5194/essd-2026-901
Preprint. Discussion started: 17 November 2026
© Author(s) 2026. CC BY 4.0 License.



Open Access Earth System Science Data Discussions

same atmospheric column. Routine radiosonde observations are also conducted at the station, providing independent vertical profiles of temperature, humidity, and wind. Radiosondes are routinely launched at 07:15 and 19:15 China Standard Time (CST) each day, reaching altitudes of approximately 30 km.

The MMCR continuously observes clouds and precipitation in a fixed, vertically pointing mode (Fig. 1c), providing Doppler spectra for velocity retrieval and radar measurements for hydrometeor classification.

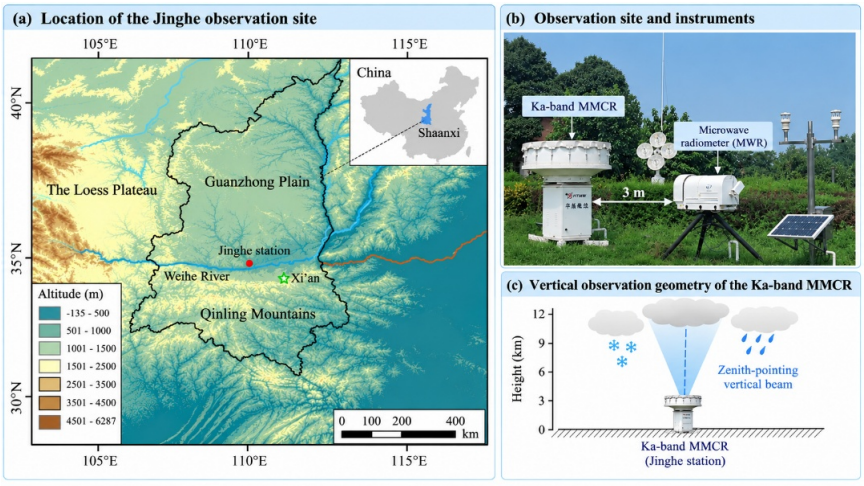



**Figure 1.** Location of the Jinghe observation site and the main observational instruments. **(a)** Location of the Jinghe station in the Guanzhong Plain, Shaanxi Province, China, and the surrounding topography. **(b)** Colocated Ka-band MMCR and MWR, separated by approximately 3 m. **(c)** Schematic of the vertically pointing observation geometry of the Ka-band MMCR.

## 2.2 Ka-band millimeter-wave cloud radar

The primary instrument used in this study is an HT101 solid-state Ka-band MMCR, which operates continuously in a fixed, vertically pointing mode; its main technical specifications are listed in Table 1. The MMCR is regularly maintained by trained personnel, and its measurements have been used in previous studies of cloud boundaries, vertical cloud structure, and cloud processes (Yuan et al., 2022a, b, 2025).

Table 1. Main technical specifications of the MMCR

| No. | Parameter | Specification |
|---|---|---|
| 1 | Radar system | Coherent pulsed Doppler radar, solid-state transmitter, pulse compression |
| 2 | Operating frequency | 35 GHz ± 200 MHz (Ka-band) |
| 3 | Scanning mode | Fixed vertical pointing (zenith) |
| 4 | Horizontal and vertical beamwidth | 0.4° × 0.4° |
| 5 | Antenna gain | 53 dB |
| 6 | Pulse repetition frequency | 5000, 6500, or 8000 Hz (adjustable) |
| 7 | Peak power | ≥20 W |
| 8 | Measured variables | $Z_e$, $V_D$, $SW$, Doppler power spectra |
| 9 | Measurement range | Height: 0.15–15 km;<br>$Z_e$: −45 to +30 dBZ;<br>$V_D$: −15 to +15 m·s$^{-1}$;<br>$SW$: 0–15 m·s$^{-1}$; |
| 10 | Temporal and vertical resolution | 5 s; 30 m |
| 11 | Pulse width | 1, 5, or 20 μs |
| 12 | Number of FFT points | 256 |

https://doi.org/10.5194/essd-2026-901
Preprint. Discussion started: 17 November 2026
© Author(s) 2026. CC BY 4.0 License.



The long-term Doppler power spectra recorded by the MMCR provide the basis for generating higher-level velocity products. In this study, $w$ is retrieved from Doppler power spectra, and $V_t$ is subsequently derived from $V_D$ and $w$. These retrieved velocities complement the conventional radar moments. All velocity variables follow a consistent sign convention, with upward motion defined as positive and downward motion as negative. Details of quality control, Doppler spectral processing, and the retrieval of $w$ and $V_t$ are provided in Appendices A and B.

### 2.3 Microwave radiometer and auxiliary observations

The MW967KA MWR is used to obtain continuous atmospheric thermodynamic profiles, and its main technical specifications are listed in Table 2. Its temperature ($T$) profiles provide the thermal constraint for hydrometeor classification. Compared with twice-daily radiosonde observations, the MWR provides continuous measurements at a temporal resolution of 2 min, enabling regular matching with MMCR measurements. During data processing, the MWR temperature profiles are mapped onto the MMCR time–height grid with a temporal resolution of 5 s and a vertical spacing of 30 m.

Table 2. Main technical specifications of the MWR

| No. | Parameter | Specification |
|---|---|---|
| 1 | Measurement range | 0–10 km |
| 2 | Vertical resolution | 25 m (0–500 m) |
| | | 50 m (500–2000 m) |
| | | 250 m (2–10 km) |
| 3 | Temporal resolution | 2 min |

## 3. Data processing and product generation

The data processing workflow consists of four steps: quality control of basic observations, retrieval of $w$ and $V_t$, hydrometeor classification, and final dataset generation (Fig. 2). Radar measurements are first quality controlled to construct a valid cloud mask; $w$ is then retrieved from Doppler spectra, and $V_t$ is calculated as $V_D$–$w$; hydrometeor classification uses $Z_e$, $V_D$, $SW$, and $T$. Finally, all variables are organized on a common time–height grid. Detailed algorithm parameters and processing procedures are provided in the Supplement.

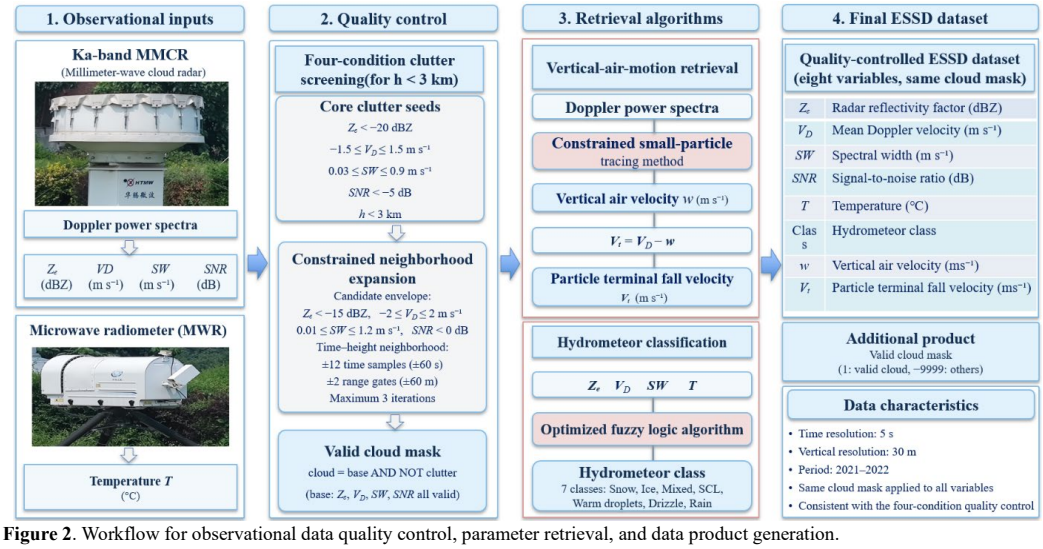



**Figure 2**. Workflow for observational data quality control, parameter retrieval, and data product generation.

https://doi.org/10.5194/essd-2026-901
Preprint. Discussion started: 17 November 2026
© Author(s) 2026. CC BY 4.0 License.



Open Access Earth System Science Data Discussions

### 3.1 Quality control of radar observations

To ensure consistency between the basic observations and subsequent retrieval products, we apply consistent quality control to $Z_e$, $V_D$, $SW$, and SNR, focusing on the removal of persistent low-level clutter below 3 km. The quality control procedure uses a core clutter seed and constrained neighborhood expansion approach to identify spatially and temporally continuous clutter within regions where all four radar variables are valid, generating a consistent valid cloud mask. This mask is applied to all subsequent data products. The specific thresholds, neighborhood expansion parameters, and batch-processing procedures are described in Appendix A.

### 3.2 Retrieval of vertical air motion and particle terminal fall velocity

For a vertically pointing MMCR, $V_D$ includes contributions from both vertical air motion and hydrometeor sedimentation and therefore cannot directly represent $w$ (Shupe et al., 2008b). In this dataset, $w$ is retrieved from Doppler power spectra using the previously developed constrained small-particle tracing method (Gossard, 1994; Shupe et al., 2008b; Yuan et al., 2026). The physical basis, constraints, and applicability of this method are detailed in Yuan et al. (2026); valid $w$ values are produced only for samples that meet these conditions during long-term processing. After retrieving $w$, $V_t$ is calculated using Eq. (1).

$$V_t = V_D - w \quad (1)$$

Throughout this study, upward velocities are defined as positive and downward velocities as negative; thus, $w > 0$ and $w < 0$ indicate upward and downward air motion, respectively, while $V_t < 0$ indicates downward hydrometeor sedimentation relative to the surrounding air. The retrieval criteria are described in Appendix B.

### 3.3 Hydrometeor classification

Hydrometeor classification is performed using the previously developed optimized fuzzy logic algorithm, using $Z_e$, $V_D$, $SW$, and $T$ as input variables. The product includes seven hydrometeor classes: Snow, Ice, Mixed, SCL, Warm droplets, Drizzle, and Rain. The membership functions, variable weights, and classification performance are detailed in Yuan et al. (2024); the same classification framework is applied to this dataset, with processing details provided in Appendix C.

### 3.4 Final dataset generation

After quality control, retrieval of $w$ and $V_t$, and hydrometeor classification, all variables are organized on a common time–height grid. The final dataset has a temporal resolution of 5 s and a vertical grid spacing of 30 m, and includes $Z_e$, $V_D$, $SW$, SNR, $T$, hydrometeor class, $w$, and $V_t$, together with a consistent valid cloud mask. Details of data integration, missing-value handling, and long-term statistical procedures are provided in Appendix D.

## 4. Dataset characteristics and quality assessment

To reduce the influence of differences in observation days and valid sample counts across months and years, consistent sample-size and altitude-range criteria are applied, and daily statistics are combined into seasonal or annual composites. Internal consistency and sensitivity analyses are used to characterize the retrieved velocity products.

### 4.1 Data coverage and product completeness

Fig. 3 shows the temporal coverage of MMCR observations and the completeness of the main data products during 2021–2022. During preprocessing, days with less than 20 h of valid data acquisition were excluded; after data processing and quality control, 541 valid observation days were retained. Daily coverage shows observational gaps in both years and high coverage on many days with available radar data (Fig. 3a). The daily coverage of valid $w$ retrievals generally follows that of the basic radar observations, with reduced coverage on some days when the retrieval conditions were not satisfied (Fig. 3b). Monthly statistics show substantial variations in radar temporal

https://doi.org/10.5194/essd-2026-901
Preprint. Discussion started: 17 November 2026
© Author(s) 2026. CC BY 4.0 License.



Open Access Earth System Science Data Discussions

coverage, while the production rates of *w* and hydrometeor classification products are generally high for valid cloud observations (Fig. 3c). The main gaps therefore reflect missing radar observations, while retrieval-product availability also varies among days.

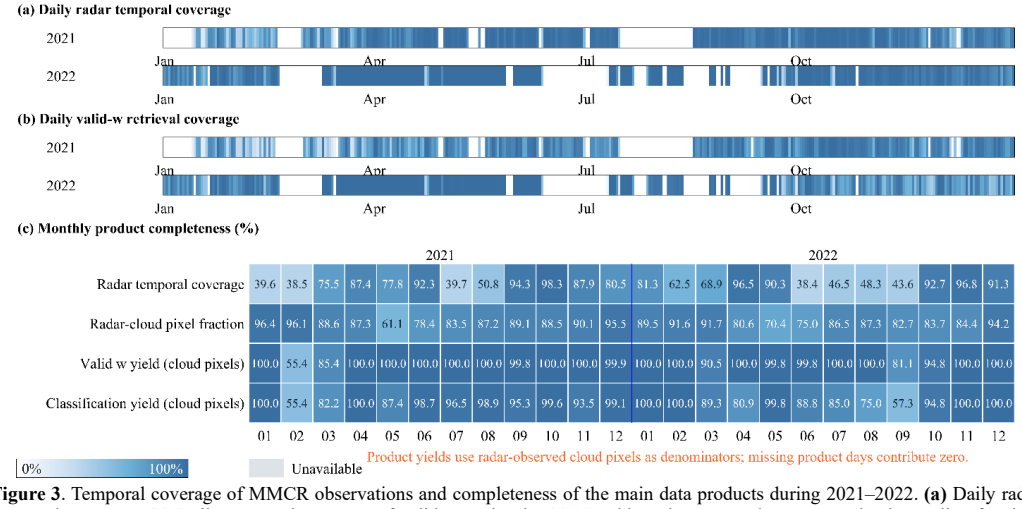



**Figure 3**. Temporal coverage of MMCR observations and completeness of the main data products during 2021–2022. **(a)** Daily radar temporal coverage. **(b)** Daily temporal coverage of valid *w* retrievals. **(c)** Monthly radar temporal coverage, cloud sampling fraction, and production rates of valid *w* and hydrometeor classification products. Gray indicates unavailable statistics. Product yields are calculated relative to the total number of valid cloud sampling points.

## 4.2 Example of the dataset products

To illustrate the dataset products, a cloud event observed on 5 February 2022 from 06:00 to 18:00 CST was selected as an example (Fig. 4). All variables retain a temporal resolution of 5 s and a vertical grid spacing of 30 m on a common time–height grid. Figs. 4a–c) show $Z_e$, $V_D$, and $SW$, respectively, while Figs. 4d–f) show $V_t$, $w$, and hydrometeor classification, respectively.

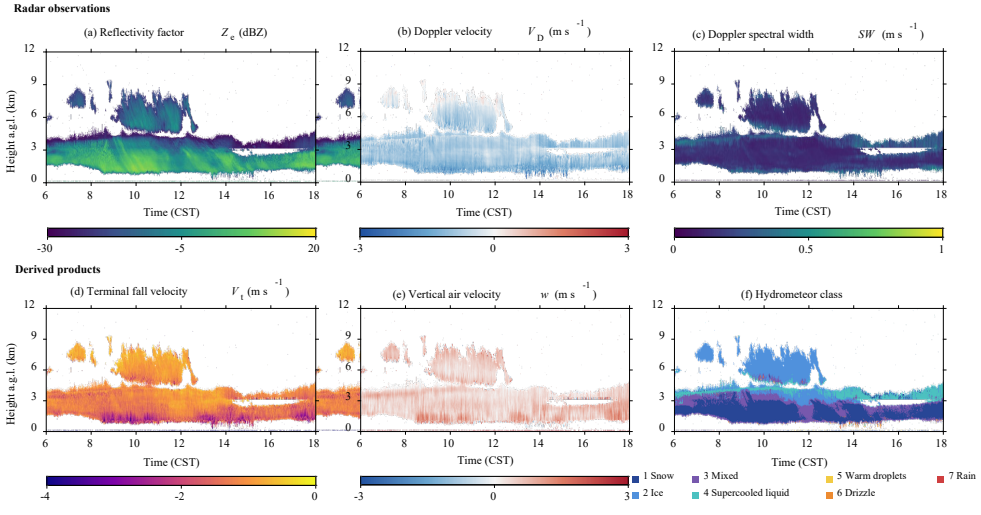



**Figure 4**. Example of MMCR observations and retrieval products on 5 February 2022. The upper panels show the basic radar products: **(a)** $Z_e$, **(b)** $V_D$, and **(c)** $SW$; the lower panels show the higher-level products: **(d)** $V_t$, **(e)** $w$, and **(f)** hydrometeor classification. Negative $V_D$ and $V_t$ indicate downward motion, while positive and negative $w$ indicate upward and downward air motion, respectively. White areas indicate missing observations or unavailable retrievals after quality control.

https://doi.org/10.5194/essd-2026-901
Preprint. Discussion started: 17 November 2026
© Author(s) 2026. CC BY 4.0 License.



Open Access Earth System Science Data Discussions

During this event, $Z_e$ shows persistent low-level cloud echoes and intermittent cloud layers at middle and upper levels, with marked differences in echo intensity across heights. $V_D$ and $SW$ generally follow the cloud structure but vary with height and time, reflecting differences in bulk particle motion and Doppler velocity dispersion among cloud regions. The retrieved $V_t$ and $w$ characterize particle sedimentation and vertical air motion, respectively. $V_t$ predominantly indicates downward sedimentation, whereas $w$ alternates between positive and negative values and exhibits finer-scale variability within clouds. The hydrometeor classification is aligned with the radar and velocity products on the same time–height grid and shows variations in hydrometeor types with height and time.

### 4.3 Statistical characteristics of vertical air motion and particle terminal fall velocity

To characterize the overall distributions of particle sedimentation and vertical air motion during 2021–2022, we calculated the probability densities of $V_t$ and $w$ and their height-dependent distributions (Fig. 5). The $V_t$ statistics include only samples with $V_t \leq 0$, excluding positive $V_t$ values found in low-SNR regions, whereas the $w$ statistics use all valid retrievals after quality control. The final numbers of samples used for the probability density analyses were $4.39\times10^8$ for $V_t$ and $4.48\times10^8$ for $w$.

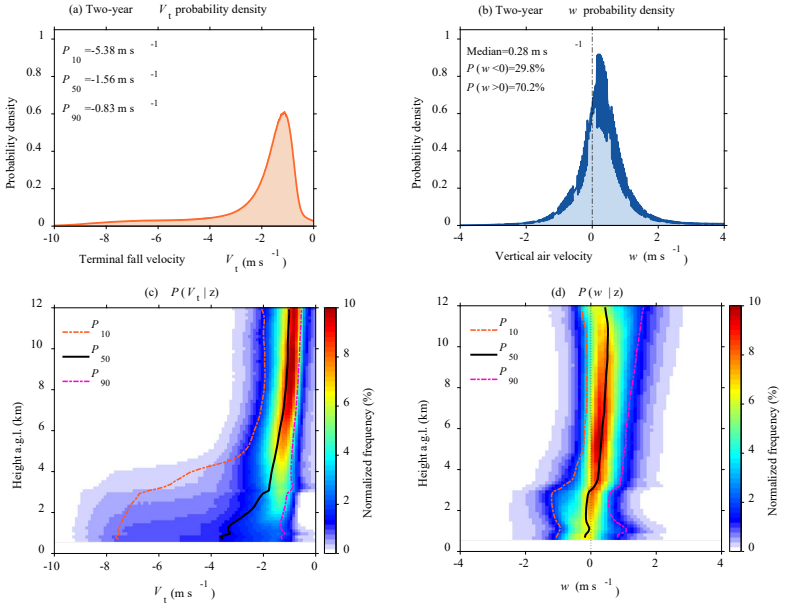



**Figure 5**. Overall probability distributions and vertical statistical characteristics of $V_t$ and $w$ during 2021–2022. **(a)** Probability density distribution of $V_t$ for all valid samples, with P10, P50, and P90 indicated. **(b)** Probability density distribution of $w$, with the dashed line indicating $w$ =0, together with the median and the fractions of samples with negative and positive $w$. **(c)** Height-dependent normalized frequency distribution of $V_t$, $P(V_t|z)$, with curves indicating P10, P50, and P90 at each height. **(d)** Height-dependent normalized frequency distribution of $w$, $P(w|z)$, with curves indicating P10, P50, and P90 at each height.

Fig. 5a) shows that $V_t$ is concentrated at relatively low to moderate sedimentation velocities, with a tail extending toward more negative values; the 10th, 50th, and 90th percentiles (P10, P50, and P90) are −5.38, −1.56, and −0.83 m·s$^{-1}$, respectively. The distribution of $w$ is more concentrated around zero (Fig. 5b), with a median of 0.28 m·s$^{-1}$; negative and positive values account for 29.8% and 70.2% of valid samples, respectively.

Figs. 5c) and 5d) further show the height-dependent conditional frequency distributions of $V_t$ and $w$, respectively. The $V_t$ distribution varies with height, showing a broader range and stronger downward

https://doi.org/10.5194/essd-2026-901
Preprint. Discussion started: 17 November 2026
© Author(s) 2026. CC BY 4.0 License.



Open Access Earth System Science Data Discussions

sedimentation at lower levels, while becoming more concentrated at lower sedimentation speeds with increasing height. In contrast, $w$ remains concentrated around zero at most heights, although its distribution width varies with height, with broader ranges of positive and negative velocities at certain levels.

### 4.4 Internal consistency and sensitivity assessment

Fig. 6 summarizes the vertical profiles of $V_D$, $V_t$, and $w$ and the monthly variation of $w$. At lower levels, the median values of $V_D$ and $V_t$ are relatively close, while $w$ remains near zero; with increasing height, $V_t$ becomes less negative and $w$ shifts toward positive values, whereas $V_D$ represents the combined contributions of air motion and particle sedimentation (Fig. 6a). Figure 6b further shows that the fractions of positive and negative $w$ vary with height: the two fractions are comparable at lower levels, while the fraction of positive $w$ increases at middle and upper levels, consistent with the predominance of positive $w$ values in Fig. 5. The monthly statistics (Figs. 6c and d) show that median $w$ varies from approximately −0.2 to 0.6 m·s$^{-1}$, remaining positive in most months but approaching zero or becoming negative in others; the fractions of positive and negative $w$ also vary across months.

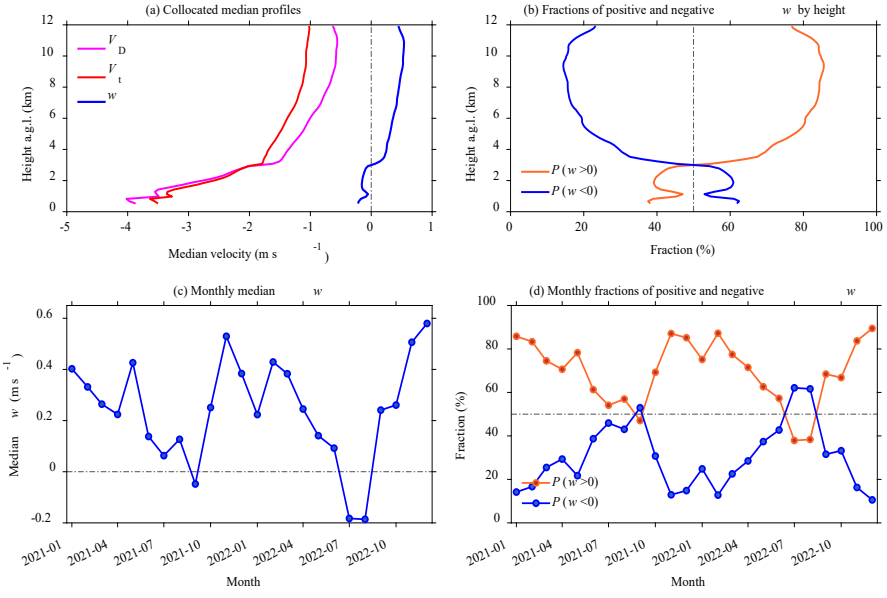



**Figure 6**. Vertical statistical characteristics of $V_D$, $V_t$, and $w$, and monthly variations in $w$ during 2021–2022. **(a)** Median vertical profiles of $V_D$, $V_t$, and $w$ calculated from collocated valid samples. **(b)** Fractions of positive and negative $w$ samples at different heights, with the gray dashed line indicating 50%. **(c)** Monthly median $w$ during 2021–2022. **(d)** Monthly fractions of positive and negative $w$ samples, with the gray dashed line indicating 50%.

Fig. 7 further examines the numerical consistency among the three velocity variables and the sensitivity of $w$ statistics to systematic offsets in $V_t$. Across the two-year dataset, 100% of the jointly valid samples have $|\varepsilon| \leq 0.01$ m·s$^{-1}$, with a median absolute residual of $1.99\times10^{-5}$ m·s$^{-1}$ and a 99th percentile of $7.31\times10^{-5}$ m·s$^{-1}$, confirming numerical closure of the velocity relationship during batch processing. The systematic perturbation test shows that an increase of approximately 0.28 m·s$^{-1}$ in $V_t$ reduces the overall median of $w$ to nearly zero and the fraction of positive $w$ samples to approximately 50%. Definitions and perturbation settings are provided in Appendix E.

https://doi.org/10.5194/essd-2026-901
Preprint. Discussion started: 17 November 2026
© Author(s) 2026. CC BY 4.0 License.

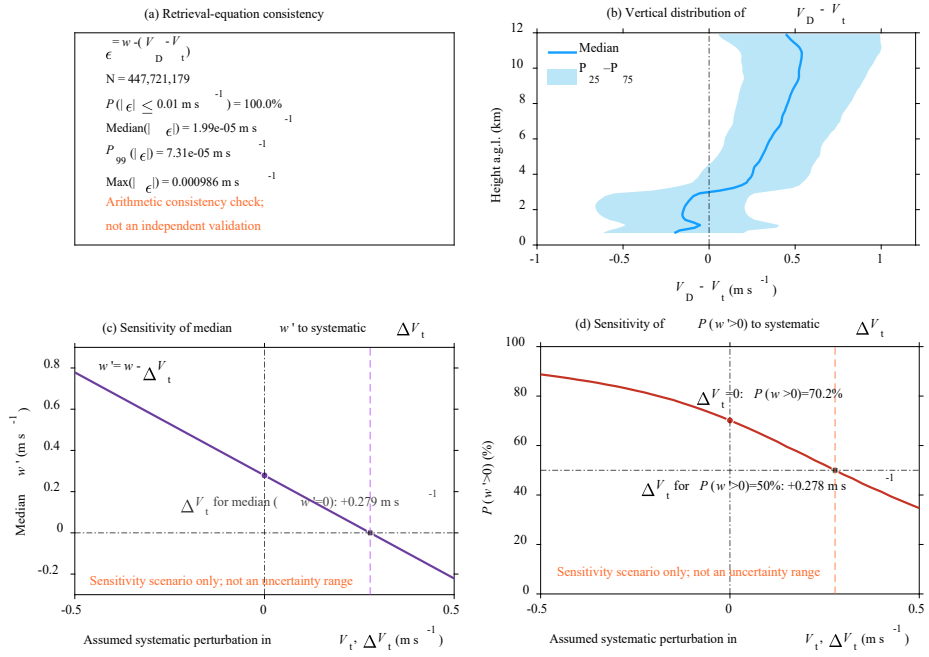



**Figure 7**. Numerical consistency of the $w$ retrieval and its sensitivity to systematic perturbations in $V_t$. **(a)** Numerical consistency check based on $w = V_D - V_t$, with the residual defined as $\varepsilon = w - (V_D - V_t)$, showing the number of valid samples and residual statistics. **(b)** Median vertical profile of $V_D - V_t$ and its interquartile range (P25–P75). **(c)** Changes in the overall median of $w' = w - \Delta V_t$ after applying an assumed systematic perturbation $\Delta V_t$ to $V_t$, with the dashed line indicating the perturbation threshold at which $w' = 0$. **(d)** Changes in the fraction of positive $w'$ samples, $P(w'>0)$, under different $\Delta V_t$ values, with the dashed line indicating the perturbation threshold at which $P(w'>0) = 50\%$.

## 4.5 Hydrometeor-dependent characteristics

Fig. 8 presents the vertical distributions of different hydrometeor classes and their corresponding $V_t$ and $w$ statistics during 2021–2022. The analysis is based on 418,818,637 time–height sampling points between 0.5 and 12 km with valid hydrometeor classification, $V_t$, and $w$. The resulting class-conditioned distributions are compared in Figs. 8a–d).

Ice exhibits higher occurrence fractions at middle and upper levels, particularly above 7 km; Mixed is most prevalent between 4 and 7 km, while Snow occurs mainly at lower and middle levels. SCL exhibits appreciable occurrence fractions at middle levels, with a vertical distribution that overlaps that of Mixed. Warm droplets, Drizzle, and Rain occur predominantly at lower levels, with Rain showing higher occurrence fractions below approximately 2.5 km.

$V_t$ varies among hydrometeor classes (Fig. 8b). Rain exhibits the highest downward sedimentation speed, with a median $V_t$ of −5.64 m·s$^{-1}$, compared with −2.07 and −1.71 m·s$^{-1}$ for Drizzle and Snow, respectively, and −1.00 m·s$^{-1}$ for Ice, which shows weaker sedimentation. The P10–P90 ranges also differ among classes, indicating variability in retrieved sedimentation velocities within each hydrometeor class. The conditional statistics of $w$ also show differences among hydrometeor classes (Figs. 8c and d). Snow and Ice have median $w$ values of 0.42 and 0.43 m·s$^{-1}$, respectively, with positive $w$ fractions of 86.47% and 87.12%. Mixed and SCL have median $w$ values of 0.31 and 0.38 m·s$^{-1}$, respectively, with positive $w$ fractions of 79.86% and 77.12%. Warm droplets and Drizzle exhibit lower

https://doi.org/10.5194/essd-2026-901
Preprint. Discussion started: 17 November 2026
© Author(s) 2026. CC BY 4.0 License.



Open Access Earth System Science Data Discussions

fractions of positive $w$, while Rain has a median $w$ of −0.45 m·s$^{-1}$ and a positive $w$ fraction of 20.05%. The median $V_t$ for SCL is −1.18 m·s$^{-1}$, representing the retrieved velocity statistic for SCL-classified. The velocity distributions of SCL-classified samples are further analyzed in Appendix F.

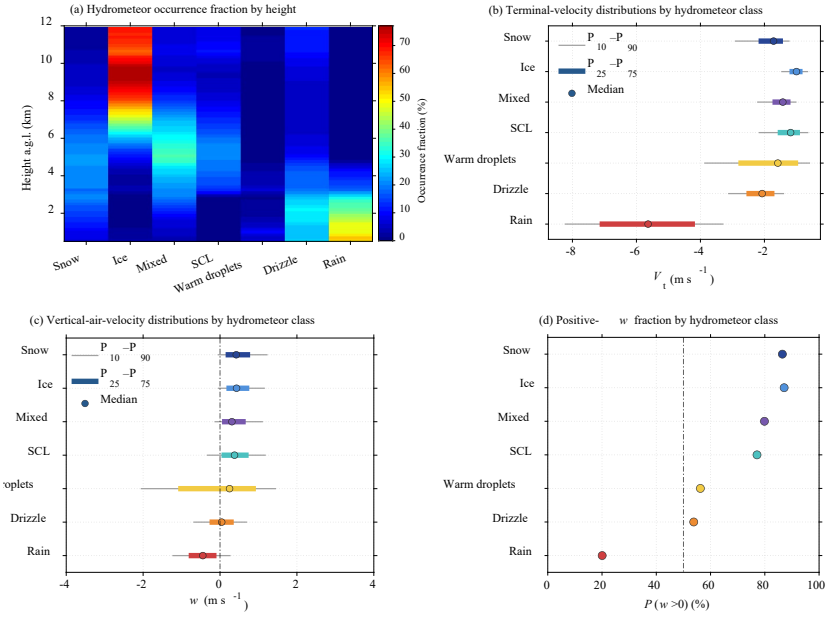



**Figure 8**. Vertical distributions of hydrometeor classes and their corresponding $V_t$ and $w$ statistics during 2021–2022. **(a)** Height-dependent occurrence fractions of seven hydrometeor classes (Snow, Ice, Mixed, SCL, Warm droplets, Drizzle, and Rain), calculated relative to the total number of valid classified samples in each height bin. **(b)** Distributions of $V_t$ for different hydrometeor classes. **(c)** Distributions of $w$ for different hydrometeor classes. **(d)** Fraction of positive $w$ samples, $P(w>0)$, for each hydrometeor class. In panels (b) and (c), circles indicate medians, while thick and thin lines represent the P25–P75 and P10–P90 ranges, respectively; the gray dashed lines in panels (c) and (d) indicate $w$ =0 and $P(w>0)$=50%, respectively. The analysis covers 0.5–12 km, with 0.15 km height bins used in panel (a); bins containing fewer than 10,000 total valid samples are shown as missing.

## 4.6 Seasonal variability

Fig. 9 presents the seasonal variability and height dependence of $w$ and $V_t$ during 2021–2022. Statistics were first calculated for individual days using 300 m height bins and then combined into seasonal composites with equal-day weighting. December–February (DJF), March–May (MAM), June–August (JJA), and September–November (SON) include 140, 152, 92, and 157 valid observation days, respectively. Seasonal differences are largest at lower and middle levels.

The median $w$ profiles differ among seasons (Fig. 9a). In DJF, median $w$ is positive at most heights, increasing with height above 6 km and exceeding 1 m·s$^{-1}$ above 9 km. Median $w$ in MAM and SON is also predominantly positive at middle and upper levels, but generally lower than in DJF. In JJA, median $w$ is lower at lower and middle levels, becoming distinctly negative near 2–3 km before gradually shifting to positive values with increasing height. The fraction of positive $w$ shows a similar seasonal pattern (Fig. 9b), decreasing to approximately 20%–30% near 2–3 km in JJA, while generally exceeding 80% at middle and upper levels in DJF. The altitude-layer statistics (Fig. 9d) further show that median $w$ in the 0.5–3 km layer is positive in DJF, MAM, and SON but negative in JJA; above 3

https://doi.org/10.5194/essd-2026-901
Preprint. Discussion started: 17 November 2026
© Author(s) 2026. CC BY 4.0 License.



Open Access Earth System Science Data Discussions

km, median $w$ is positive in all four seasons. The low-level $w$ statistics for JJA were examined separately for each year, with median $w$ values of −0.378 and −0.132 m·s$^{-1}$ in the 0.5–3 km layer for 2021 and 2022, respectively, both showing negative values. The main seasonal patterns remained consistent when the height-bin size was reduced from 300 to 150 m, with similar seasonal patterns in both cases.

Seasonal differences in $V_t$ are most pronounced at lower and middle levels (Fig. 9c). In JJA, stronger downward sedimentation occurs near 2–3 km, with median $V_t$ below −4 m·s$^{-1}$, whereas weaker sedimentation is observed in the other seasons. With increasing height, the seasonal $V_t$ profiles gradually converge, with median values at upper levels mainly ranging from −1.0 to −1.5 m·s$^{-1}$. Seasonal median 0 °C isotherm heights are shown for reference.

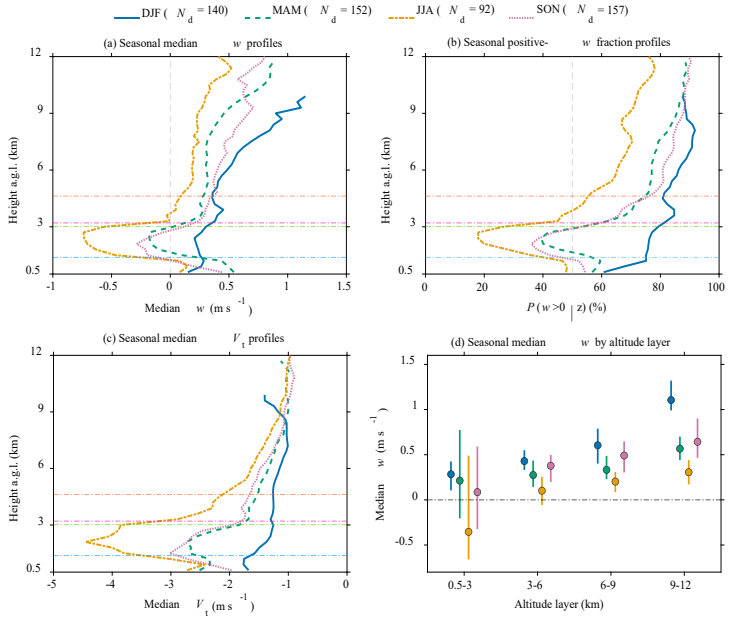



**Figure 9**. Seasonal variability and height dependence of $w$ and $V_t$ during 2021–2022. **(a)** Seasonal median vertical profiles of $w$. **(b)** Seasonal vertical profiles of the positive-$w$ fraction, $P(w>0 \mid z)$, with the gray dashed line indicating 50%. **(c)** Seasonal median vertical profiles of $V_t$. **(d)** Seasonal statistics of $w$ within four altitude layers (0.5–3, 3–6, 6–9, and 9–12 km), where circles indicate the seasonal medians of daily median $w$, and vertical bars represent the P25–P75 ranges of the daily medians. All seasonal statistics were calculated using 300 m height bins and equal-day-weighted composites of daily statistics. The color-matched horizontal dashed lines in panels (a)–(c) indicate the representative seasonal heights of the 0 °C isotherm derived from MWR temperature profiles.

## 4.7 Interannual consistency

Fig. 10 compares the vertical statistical characteristics of $w$, $V_t$, and the fraction of positive $w$ samples between 2021 and 2022. The statistics were calculated using 300 m height bins and equal-day-weighted composites to reduce the influence of differences in sample counts among observation days on the annual results. The vertical distributions of valid observation days are similar between the two years (Fig. 10a). Between approximately 0.5 and 9 km, most heights have sufficient sampling support, with slightly more valid observation days in 2021 than in 2022. Both years show a local decrease in valid observation days near 2–3 km, while the number of valid days decreases markedly with height above 9 km, where fewer observation days contribute to the annual profiles.

The median $w$ profiles exhibit similar vertical patterns in both years (Fig. 10b). In both years, median $w$ decreases markedly near 2–3 km, with more negative values in 2021; above 3 km, median $w$ generally increases with height, and the two profiles are similar at middle and upper levels. The fraction of positive $w$ shows a similar vertical pattern

https://doi.org/10.5194/essd-2026-901
Preprint. Discussion started: 17 November 2026
© Author(s) 2026. CC BY 4.0 License.





(Fig. 10c), reaching a minimum near 2–3 km before increasing with height to approximately 70%–90% at middle and upper levels. Based on 39 height bins with valid data in both years, the correlations between the 2021 and 2022 profiles are 0.890 for median $w$ and 0.956 for $P(w>0\,|\,z)$.

The median $V_t$ profiles exhibit similar vertical patterns in 2021 and 2022 (Fig. 10d). Both years show stronger downward sedimentation at lower levels, with sedimentation speeds decreasing with height and the profiles becoming more similar above 3 km. The correlation between the annual median $V_t$ profiles is 0.964, with a median absolute difference of 0.120 $m \cdot s^{-1}$; the largest differences occur at lower levels.

To assess the influence of sampling support on the interannual comparison, we further restricted the analysis to height bins with at least 30 valid observation days in both 2021 and 2022. After this restriction, the correlations between the 2021 and 2022 profiles were 0.956, 0.980, and 0.964 for $w$, $P(w>0\,|\,z)$ and $V_t$, respectively. Compared with the results based on all height bins with valid data in both years, the correlations increased for $w$ and $P(w>0\,|\,z)$, while that for $V_t$ remained nearly unchanged, showing similar vertical patterns when the comparison is restricted to well-sampled heights.

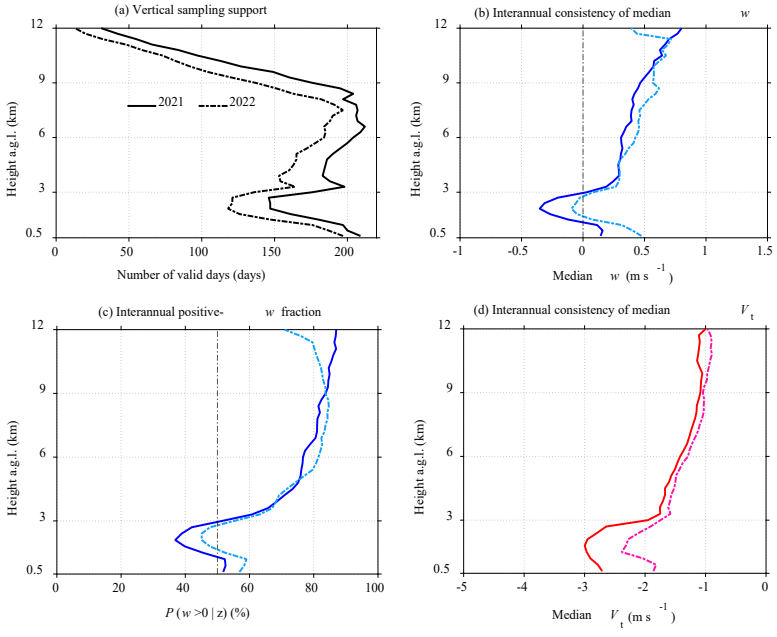



**Figure 10**. Vertical sampling support and interannual consistency of the retrieved velocity products in 2021 and 2022. **(a)** Number of valid observation days at different heights in 2021 and 2022. **(b)** Median vertical profiles of $w$ for the two years. **(c)** Vertical profiles of the positive-$w$ fraction, $P(w>0\,|\,z)$, for the two years, with the gray dashed line indicating 50%. **(d)** Median vertical profiles of $V_t$ for the two years. Solid and dashed lines represent 2021 and 2022, respectively. The long-term vertical statistics were calculated using consistent 300 m height bins and equal-day-weighted composites of daily statistics to reduce the influence of differences in observation duration among days on the annual results.

## 5. Data availability

The dataset presented in this study is publicly available at https://doi.org/10.57760/sciencedb.016rz (Di et al., 2026). It contains quality-controlled MMCR observations ($Z_e$, $V_D$, $SW$, and SNR), MWR temperature profiles ($T$), retrieved velocity products ($w$ and $V_t$), and seven-category hydrometeor classification, together with a valid cloud

https://doi.org/10.5194/essd-2026-901
Preprint. Discussion started: 17 November 2026
© Author(s) 2026. CC BY 4.0 License.



Open Access Earth System Science Data Discussions

mask. The dataset covers 541 valid observation days during 2021–2022, with a temporal resolution of 5 s and a vertical grid spacing of 30 m. All variables are provided on a common time–height grid to facilitate their combined use.

## 6. Conclusions

Using Ka-band MMCR and MWR observations collected at the Jinghe station in Xi'an during 2021–2022, we developed a high-resolution dataset integrating conventional radar measurements, vertical air velocity ($w$), particle terminal fall velocity ($V_t$), and hydrometeor classification. The $w$ product was retrieved from MMCR Doppler power spectra, and $V_t$ was calculated from the mean Doppler velocity and $w$. Seven hydrometeor classes were identified using radar measurements and temperature profiles. After quality control and data integration, the final dataset contains 541 valid observation days, with a temporal resolution of 5 s and a vertical grid spacing of 30 m.

The two-year statistics show distinct vertical and temporal variations in $w$ and $V_t$. The overall median $V_t$ and $w$ are −1.56 and 0.28 m·s$^{-1}$, respectively, with positive w accounting for 70.2% of valid samples. Velocity distributions also differ among hydrometeor classes. Rain exhibits stronger downward sedimentation and a lower fraction of positive $w$, while Snow and Ice show weaker sedimentation and higher fractions of positive $w$. Seasonal differences are most pronounced at lower and middle levels, with JJA showing lower $w$ and stronger downward sedimentation near 2–3 km.

The velocity products exhibit similar vertical statistical patterns in 2021 and 2022. The correlations between the annual profiles of median $w$, the fraction of positive $w$, and median $V_t$ are 0.890, 0.956, and 0.964, respectively. When the analysis is restricted to height bins containing at least 30 valid observation days in both years, the corresponding correlations are 0.956, 0.980, and 0.964, indicating similar vertical statistical patterns at heights with sufficient observational coverage. Numerical consistency and sensitivity analyses further characterize the relationships among the velocity products and their statistical properties.

By integrating Doppler-spectrum-derived velocity products with conventional radar measurements and hydrometeor classification on a common time–height grid, the dataset provides long-term observations for studies of cloud vertical structure, vertical air motion, particle sedimentation, and cloud-to-precipitation transitions.

## Appendix A. Quality control of MMCR observations

We first apply consistent quality control to $Z_e$, $V_D$, $SW$, and SNR. Values of −9999 and non-finite values in the original data are treated as missing, and only time–height sampling points where all four radar variables are simultaneously valid are retained. Examination of the long-term observations shows that anomalous signals occur mainly below 3 km and are typically characterized by low $Z_e$, low SNR, near-zero $V_D$, and narrow $SW$; therefore, low-level clutter is identified using core clutter seeds followed by constrained neighborhood expansion.

Core clutter seeds are restricted to heights below 3 km and satisfy $Z_e < -20$ dBZ, $-1.5 \le V_D \le 1.5$ m·s$^{-1}$, $0.03 \le SW \le 0.9$ m·s$^{-1}$, and SNR < −5 dB. Candidate points for neighborhood expansion satisfy $Z_e < -15$ dBZ, $-2 \le V_D \le 2$ m·s$^{-1}$, $0.01 \le SW \le 1.2$ m·s$^{-1}$, and SNR < 0 dB. The expansion uses a time–height neighborhood of approximately ±60 s and ±60 m for up to three iterations.

The final valid cloud mask is generated by excluding the identified low-level clutter from time–height sampling points where all four radar variables are valid and is applied consistently to all subsequent data products. The same quality control parameters are applied to all observation days during 2021–2022 to ensure consistent processing throughout the observation period.

https://doi.org/10.5194/essd-2026-901
Preprint. Discussion started: 17 November 2026
© Author(s) 2026. CC BY 4.0 License.



Open Access Earth System Science Data Discussions

## Appendix B. Retrieval of vertical air motion and particle terminal fall velocity

In this dataset, $w$ is retrieved using the previously developed constrained small-particle tracing method. Previous work systematically examined the tracer spectral-point echo intensity ($Z_{first}$), the minimum valid echo intensity ($Z_{least}$), and spectral width thresholds for different hydrometeor phases, and established the applicability criteria for the method (Yuan et al., 2026).

Valid $w$ estimates are produced only for Doppler spectra that satisfy the applicability criteria of the constrained small-particle tracing method; other samples are marked as missing. Although Yuan et al. (2026) also described a method for separable bimodal Doppler spectra, that method was not used in this dataset. The constrained small-particle tracing method was applied consistently across all observation days. $V_t$ was then calculated as $V_D - w$.

## Appendix C. Hydrometeor classification

Hydrometeor classification is performed using the optimized fuzzy logic algorithm previously developed by the authors, with $Z_e$, $V_D$, $SW$, and $T$ as input variables (Yuan et al., 2024). The method assigns membership functions to each hydrometeor class, calculates the combined membership score using the weights of the input variables, and assigns each time–height sampling point to the class with the highest combined membership score. Optimized asymmetric T-shaped membership functions are used to reduce misclassification caused by overlapping radar characteristics among hydrometeor classes.

The classification framework, membership functions, weights, and parameter settings are described in Yuan et al. (2024), where near-surface classification results were compared with observations from a colocated present weather sensor, showing good agreement in precipitation types.

## Appendix D. Final dataset generation and statistical procedures

The MMCR and MWR products are organized on a common time–height grid with a temporal resolution of 5 s and a vertical grid spacing of 30 m; no additional vertical interpolation is applied to the radar variables. Missing codes (−9999) and non-finite values are treated as missing. Days with less than 20 h of data acquisition are excluded from the retained dataset, leaving 541 observation days. The released variables are $Z_e$, $V_D$, $SW$, SNR, $T$, hydrometeor class, $w$, and $V_t$ together with the valid cloud mask.

Seasonal and interannual velocity profiles are first calculated for each observation day using 300 m height bins, followed by equal-day-weighted composites. Daily height bins require at least 1000 valid samples, and seasonal height bins require at least 10 contributing days. Hydrometeor occurrence fractions in Fig. 8a) use 0.15 km height bins, with bins containing fewer than 10,000 valid classified samples shown as missing. The class-conditioned velocity statistics use jointly valid classification, $w$, and $V_t$ samples between 0.5 and 12 km.

## Appendix E. Internal consistency and sensitivity analyses

Numerical consistency is assessed using $\varepsilon = w - (V_D - V_t)$ for samples with all three velocity variables available. Across 447,721,179 jointly valid samples, the fraction with $|\varepsilon| \leq 0.01$ m·s$^{-1}$ is 100%; the median and 99th percentile of $|\varepsilon|$ are $1.99 \times 10^{-5}$ and $7.31 \times 10^{-5}$ m·s$^{-1}$, respectively. For the sensitivity analysis, an assumed systematic offset $\Delta V_t$ is added to $V_t$, yielding $w' = V_D - (V_t + \Delta V_t) = w - \Delta V_t$. The median $w'$ approaches zero at $\Delta V_t \approx +0.279$ m·s$^{-1}$, and the fraction of positive $w'$ samples reaches 50% at $\Delta V_t \approx +0.278$ m·s$^{-1}$.

https://doi.org/10.5194/essd-2026-901
Preprint. Discussion started: 17 November 2026
© Author(s) 2026. CC BY 4.0 License.

Open Access Earth System Science Data Discussions

## Appendix F. Diagnostic analysis for SCL-classified samples

Among the hydrometeor classes, SCL has a median $V_t$ of approximately −1.18 m·s$^{-1}$. To further characterize the velocity statistics of SCL-classified samples, we examined variations with $Z_e$, vertical velocity profiles, and relationships among the velocity components (Fig. F1).

Based on the $Z_e$ distribution, all valid SCL-classified samples were divided into four quartile groups (Q1–Q4), each containing approximately 25% of the samples (Fig. F1a). With increasing$Z_e$, median $w$ increases from 0.31 to 0.51 m·s$^{-1}$, and median $V_D$ shifts from −0.77 to −0.58 m·s$^{-1}$, while median $V_t$ values are −1.20, −1.20, −1.18, and −1.14 m·s$^{-1}$ for Q1–Q4, respectively. Median $V_t$ varies little among the reflectivity quartiles, with no clear increase in sedimentation speed as $Z_e$ increases.

Fig. F1b further presents the median vertical profiles of $V_D$, $w$, and $V_t$ for SCL-classified samples. Between approximately 3 and 11 km, median $V_t$ remains mainly between −1.2 and −1.1 m·s$^{-1}$, while $V_D$ and $w$ exhibit different vertical variations. Some range gates at lower and upper levels contain fewer than 10,000 valid samples, and the corresponding profile segments are shown in lighter colors. Median $V_t$ values for SCL remain within a similar range across multiple height levels with sufficient sampling support.

Fig. F1c shows the joint frequency distribution of $V_D$ and $w$ for SCL-classified samples. The highest frequencies occur mainly where $V_D$ <0 and $w$ is positive or near zero, indicating that $V_D$ is predominantly negative, whereas retrieved $w$ is often positive or close to zero. According to $V_t = V_D - w$, the line $w = V_D$ corresponds to $V_t$ =0, while $w > V_D$ corresponds to $V_t$ <0. This joint distribution illustrates the statistical relationship between the observed $V_D$ and retrieved $w$ for SCL-classified samples.

These analyses show that median $V_t$ for SCL-classified samples varies little across reflectivity quartiles and different height ranges. Hydrometeor classification and velocity retrieval products characterize the hydrometeor class and motion characteristics, respectively, at each radar sampling point. The SCL-conditioned $V_t$ statistics describe the retrieved sedimentation velocities at samples classified as SCL.

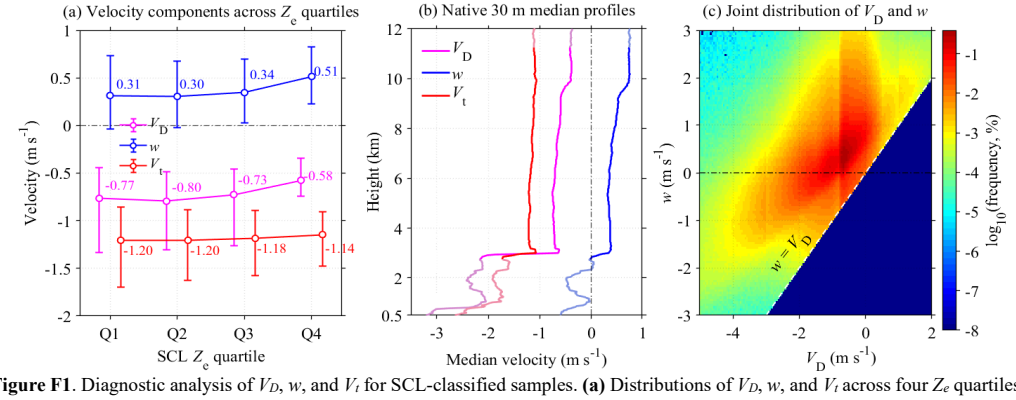



**Figure F1**. Diagnostic analysis of $V_D$, $w$, and $V_t$ for SCL-classified samples. **(a)** Distributions of $V_D$, $w$, and $V_t$ across four $Z_e$ quartiles of SCL-classified samples. Q1–Q4 each contain approximately 25% of the valid SCL samples, representing progressively stronger radar echoes; circles indicate medians, and error bars represent the P25–P75 ranges. **(b)** Median vertical profiles of $V_D$, $w$, and $V_t$ for SCL-classified samples at the native vertical resolution. Dark-colored segments indicate range gates with N≥10,000 valid SCL samples, while light-colored segments indicate range gates with N<10,000. **(c)** Joint frequency distribution of $V_D$ and $w$ for SCL-classified samples. The white dashed line $w = V_D$ corresponds to $V_t$ =0, while the horizontal dotted line indicates $w$ =0. The quartiles are defined from the $Z_e$ distribution of all valid SCL samples: Q1, $Z_e \leq -23.725$ dBZ; Q2, $-23.725 < Z_e \leq -21.125$ dBZ; Q3, $-21.125 < Z_e \leq -18.625$dBZ; and Q4, $Z_e > -18.625$ dBZ. Q1–Q4 represent reflectivity quartiles within the SCL class rather than distinct hydrometeor classes.

https://doi.org/10.5194/essd-2026-901
Preprint. Discussion started: 17 November 2026
© Author(s) 2026. CC BY 4.0 License.



Open Access Earth System Science Data Discussions

## Author contributions.

Huige Di and Yun Yuan wrote the manuscript. Yun Yuan developed and implemented the retrieval algorithms. Shuling Hu collected and organized the observational data. Ning Chen standardized the data product formats. Yufeng Wang and Qing Yan coordinated the field observations. Huige Di and Dengxin Hua reviewed the manuscript and supervised its preparation. Huige Di, Yun Yuan, and Dengxin Hua provided funding support for this study.

## Competing interests.

The authors declare that they have no competing interests.

## Financial support.

This study was supported by the National Natural Science Foundation of China (grant nos. 42130612 (Huige Di), 42427804 (Dengxin Hua), and 42505134 (Yun Yuan)), the Natural Science Basic Research Program of Shaanxi (grant no. 2025JC-YBQN-453 (Yun Yuan)), and the Shaanxi Province Postdoctoral Research Project (grant no. 2025BSHSDZZ301 (Yun Yuan))

## Acknowledgements

The authors thank the Xi'an Meteorological Bureau and the staff of the Jinghe Atmospheric Observation Center, particularly Mei Cao, Danyang Ren, and Yiwei Liu, for their regular maintenance and inspection of the observational instruments. Their support contributed to the continuity of the observations and the development of this dataset.

During the preparation of this manuscript, ChatGPT was used to assist with English translation and language refinement during manuscript preparation. The authors reviewed and revised the translated text.

## References

Acquistapace, C., Coulter, R., Crewell, S., Garcia-Benadi, A., Gierens, R., Labbri, G., Myagkov, A., Risse, N., and Schween, J. H.: EUREC4A's Maria S. Merian ship-based cloud and micro rain radar observations of clouds and precipitation, Earth Syst. Sci. Data, 14, 33–55, https://doi.org/10.5194/essd-14-33-2022, 2022.

Bühl, J., Leinweber, R., Görsdorf, U., Radenz, M., Ansmann, A., and Lehmann, V.: Combined vertical-velocity observations with Doppler lidar, cloud radar and wind profiler, Atmos. Meas. Tech., 8, 3527–3536, https://doi.org/10.5194/amt-8-3527-2015, 2015.

Bühl, J., Seifert, P., Myagkov, A., and Ansmann, A.: Measuring ice- and liquid-water properties in mixed-phase cloud layers at the Leipzig Cloudnet station, Atmos. Chem. Phys., 16, 10609–10620, https://doi.org/10.5194/acp-16-10609-2016, 2016.

Chellini, G., Gierens, R., Ebell, K., Kiszler, T., Krobot, P., Myagkov, A., Schemann, V., and Kneifel, S.: Low-level mixed-phase clouds at the high Arctic site of Ny-Ålesund: a comprehensive long-term dataset of remote sensing observations, Earth Syst. Sci. Data, 15, 5427–5448, https://doi.org/10.5194/essd-15-5427-2023, 2023.

Di, H. G., Yuan, Y., and Hua, D. X.: Remote sensing dataset of in-cloud vertical air motion, particle terminal fall velocity, and hydrometeor classification over Xi'an, China [DS/OL]. V1. Science Data Bank, 2026[2026-11-03]. https://doi.org/10.57760/sciencedb.016rz. DOI:10.57760/sciencedb.016rz.

Ferrone, A. and Berne, A.: Radar and ground-level measurements of clouds and precipitation collected during the POPE 2020 campaign at Princess Elisabeth Antarctica, Earth Syst. Sci. Data, 15, 1115–1132, https://doi.org/10.5194/essd-15-1115-2023, 2023.

Görsdorf, U., Lehmann, V., Bauer-Pfundstein, M., Peters, G., Vavriv, D., Vinogradov, V., and Volkov, V.: A 35-GHz polarimetric Doppler radar for long-term observations of cloud parameters—description of system and data processing, J. Atmos. Ocean. Technol., 32, 675–690, https://doi.org/10.1175/JTECH-D-14-00066.1, 2015.

Gossard, E. E.: Measurement of cloud droplet size spectra by Doppler radar, J. Atmos. Ocean. Technol., 11, 712–726,

https://doi.org/10.5194/essd-2026-901
Preprint. Discussion started: 17 November 2026
© Author(s) 2026. CC BY 4.0 License.





https://doi.org/10.1175/1520-0426(1994)011<0712:MOCDSS>2.0.CO;2, 1994.

Illingworth, A. J., Hogan, R. J., O'Connor, E. J., Bouniol, D., Brooks, M. E., Delanoë, J., Donovan, D. P., Eastment, J. D., Gaussiat, N., Goddard, J. W. F., Haeffelin, M., Klein Baltink, H., Krasnov, O. A., Pelon, J., Piriou, J.-M., Protat, A., Russchenberg, H. W. J., Seifert, A., Tompkins, A. M., van Zadelhoff, G.-J., Vinit, F., Willén, U., Wilson, D. R., and Wrench, C. L.: Cloudnet: continuous evaluation of cloud profiles in seven operational models using ground-based observations, Bull. Amer. Meteor. Soc., 88, 883–898, https://doi.org/10.1175/BAMS-88-6-883, 2007.

Kollias, P., Albrecht, B. A., Lhermitte, R., and Savtchenko, A.: Radar observations of updrafts, downdrafts, and turbulence in fair-weather cumuli, J. Atmos. Sci., 58, 1750–1766, https://doi.org/10.1175/1520-0469(2001)058<1750:ROOUDA>2.0.CO;2, 2001.

Kollias, P., Albrecht, B. A., and Marks, F. D.: Why Mie? Accurate observations of vertical air velocities and raindrops using a cloud radar, Bull. Amer. Meteor. Soc., 83, 1471–1484, https://doi.org/10.1175/BAMS-83-10-1471, 2002.

Kollias, P., Miller, M. A., Luke, E. P., Johnson, K. L., Clothiaux, E. E., Moran, K. P., Widener, K. B., and Albrecht, B. A.: The Atmospheric Radiation Measurement Program cloud profiling radars: second-generation sampling strategies, processing, and cloud data products, J. Atmos. Ocean. Technol., 24, 1199–1214, https://doi.org/10.1175/JTECH2033.1, 2007a.

Kollias, P., Clothiaux, E. E., Miller, M. A., Albrecht, B. A., Stephens, G. L., and Ackerman, T. P.: Millimeter-wavelength radars: new frontier in atmospheric cloud and precipitation research, Bull. Amer. Meteor. Soc., 88, 1608–1624, https://doi.org/10.1175/BAMS-88-10-1608, 2007b.

Kollias, P., Rémillard, J., Luke, E., and Szyrmer, W.: Cloud radar Doppler spectra in drizzling stratiform clouds: 1. Forward modeling and remote sensing applications, J. Geophys. Res.-Atmos., 116, D13201, https://doi.org/10.1029/2010JD015237, 2011a.

Kollias, P., Szyrmer, W., Rémillard, J., and Luke, E.: Cloud radar Doppler spectra in drizzling stratiform clouds: 2. Observations and microphysical modeling of drizzle evolution, J. Geophys. Res.-Atmos., 116, D13203, https://doi.org/10.1029/2010JD015238, 2011b.

Liu, L. P., Xie, L., and Cui, Z. H.: Examination and application of Doppler spectral density data in drop size distribution retrieval in weak precipitation by cloud radar, Chinese J. Atmos. Sci., 38, 223–236, https://doi.org/10.3878/j.issn.1006-9895.2013.12207, 2014.

Liu, L., Zheng, J., and Wu, J.: A Ka-band solid-state transmitter cloud radar and data merging algorithm for its measurements, Adv. Atmos. Sci., 34, 545–558, https://doi.org/10.1007/s00376-016-6044-8, 2017.

Liu, L. P., Ding, H., Dong, X. B., Cao, J. W., and Su, T.: Applications of QC and merged Doppler spectral density data from Ka-band cloud radar to microphysics retrieval and comparison with airplane in situ observation, Remote Sens., 11, 1595, https://doi.org/10.3390/rs11131595, 2019.

Luke, E. P. and Kollias, P.: Separating cloud and drizzle radar moments during precipitation onset using Doppler spectra, J. Atmos. Ocean. Technol., 30, 1656–1671, https://doi.org/10.1175/JTECH-D-11-00195.1, 2013.

North, K. W., Oue, M., Kollias, P., Giangrande, S. E., Collis, S. M., and Potvin, C. K.: Vertical air motion retrievals in deep convective clouds using the ARM scanning radar network in Oklahoma during MC3E, Atmos. Meas. Tech., 10, 2785–2806, https://doi.org/10.5194/amt-10-2785-2017, 2017.

O'Connor, E. J., Hogan, R. J., and Illingworth, A. J.: Retrieving stratocumulus drizzle parameters using Doppler radar and lidar, J. Appl. Meteorol., 44, 14–27, https://doi.org/10.1175/JAM-2181.1, 2005.

Peng, L., Chen, H. B., and Li, B.: An application of fuzzy logic method to cloud hydrometeor classifications using the ARM WACR data, Remote Sens. Technol. Appl., 26, 655–663, https://doi.org/10.11873/j.issn.1004-0323.2011.5.655, 2011.

Radenz, M., Bühl, J., Lehmann, V., Görsdorf, U., and Leinweber, R.: Combining cloud radar and radar wind profiler for a value added estimate of vertical air motion and particle terminal velocity within clouds, Atmos. Meas. Tech., 11, 5925–5940, https://doi.org/10.5194/amt-11-5925-2018, 2018.

Shupe, M. D., Kollias, P., Matrosov, S. Y., and Schneider, T. L.: Deriving mixed-phase cloud properties from Doppler radar spectra, J. Atmos. Ocean. Technol., 21, 660–670, https://doi.org/10.1175/1520-0426(2004)021<0660:DMCPFD>2.0.CO;2, 2004.

https://doi.org/10.5194/essd-2026-901
Preprint. Discussion started: 17 November 2026
© Author(s) 2026. CC BY 4.0 License.





Shupe, M. D., Kollias, P., Persson, P. O. G., and McFarquhar, G. M.: Vertical motions in Arctic mixed-phase stratiform clouds, J. Atmos. Sci., 65, 1304–1322, https://doi.org/10.1175/2007JAS2479.1, 2008a.

Shupe, M. D., Kollias, P., Poellot, M., and Eloranta, E.: On deriving vertical air motions from cloud radar Doppler spectra, J. Atmos. Ocean. Technol., 25, 547–557, https://doi.org/10.1175/2007JTECHA1007.1, 2008b.

Tukiainen, S., Siipola, T., Leskinen, N., and O'Connor, E.: Remote sensing measurements during PaCE 2022 campaign, Earth Syst. Sci. Data, 17, 3797–3806, https://doi.org/10.5194/essd-17-3797-2025, 2025.

Vogl, T., Radenz, M., Ramelli, F., Gierens, R., and Kalesse-Los, H.: PEAKO and peakTree: tools for detecting and interpreting peaks in cloud radar Doppler spectra – capabilities and limitations, Atmos. Meas. Tech., 17, 6547–6568, https://doi.org/10.5194/amt-17-6547-2024, 2024.

Williams, C. R., Beauchamp, R. M., and Chandrasekar, V.: Vertical air motions and raindrop size distributions estimated using mean Doppler velocity difference from 3- and 35-GHz vertically pointing radars, IEEE Trans. Geosci. Remote Sens., 54, 6048–6060, https://doi.org/10.1109/TGRS.2016.2580526, 2016.

Yu, G., Verlinde, J., Clothiaux, E. E., and Chen, Y.-S.: Mixed-phase cloud phase partitioning using millimeter wavelength cloud radar Doppler velocity spectra, J. Geophys. Res.-Atmos., 119, 7556–7576, https://doi.org/10.1002/2013JD021182, 2014.

Yuan, Y., Di, H. G., Liu, Y. Y., Yang, T., Li, Q. M., Yan, Q., Xin, W. H., Li, S. C., and Hua, D. X.: Detection and analysis of cloud boundary in Xi'an, China, employing 35 GHz cloud radar aided by 1064 nm lidar, Atmos. Meas. Tech., 15, 4989–5006, https://doi.org/10.5194/amt-15-4989-2022, 2022a.

Yuan, Y., Di, H. G., Liu, Y. Y., Cheng, D. M., Chen, N., Yan, Q., and Hua, D. X.: Confidence and error analyses of the radiosonde and Ka-wavelength cloud radar for detecting the cloud vertical structure, Remote Sens., 14, 4462, https://doi.org/10.3390/rs14184462, 2022b.

Yuan, Y., Di, H. G., Gao, Y. X., Cao, M., and Hua, D. X.: Optimization algorithm for recognizing phase states of cloud particles based on fuzzy logic, Acta Opt. Sin., 44, 1201010, https://doi.org/10.3788/AOS231598, 2024.

Yuan, Y., Di, H. G., and Hua, D. X.: Microphysical processes and enhancement effect of natural seeder–feeder in stratiform snowfall observed by millimeter-wave cloud radar, IEEE Trans. Geosci. Remote Sens., 63, 1–16, https://doi.org/10.1109/TGRS.2024.3525010, 2025.

Yuan, Y., Di, H. G., Wang, J. L., and Hua, D. X.: Research on the inversion method of vertical airflow motion in complex phase layered clouds, Atmos. Res., 336, 108843, https://doi.org/10.1016/j.atmosres.2026.108843, 2026.

Zheng, J., Liu, L., Zhu, K., Wu, J., and Wang, B.: A method for retrieving vertical air velocities in convective clouds over the Tibetan Plateau from TIPEX-III cloud radar Doppler spectra, Remote Sens., 9, 964, https://doi.org/10.3390/rs9090964, 2017.

Zhu, Z., Kollias, P., Yang, F., and Luke, E.: On the estimation of in-cloud vertical air motion using radar Doppler spectra, Geophys. Res. Lett., 48, e2020GL090682, https://doi.org/10.1029/2020GL090682, 2021.